A Hierarchical Three-Dimensional Multiscale Electro–Magneto–Thermal Model of Quenching in $REBa_2Cu_3O_{7-\delta}$ Coated-Conductor-Based Coils

Wan Kan Chan, *Member, IEEE*, and Justin Schwartz, *Fellow, IEEE*

***Abstract*—Quench detection and protection in $REBa_2Cu_3O_{7-\delta}$ (REBCO) coated conductor (CC)-based superconducting magnets is difficult due to slow normal zone propagation velocity and the multilayer composite architecture of the conductor. To design effective quench detection and protection methods, it is essential to know the electrical, thermal, and structural behavior during the quench at multiple length scales ranging from the micrometer scale within the layers of the conductor to the macroscopic behavior of the coil. Here, a hierarchical multiscale approach is used to develop a modular 3-D electro–magneto–thermal coil quench model. The model uses an accurate experimentally validated micrometer-scale REBCO CC model as the basic building block. The CC model is embedded within a homogenized coil framework at one or more locations in the form of multilayer tape modules. This multiscale approach makes possible the studies of quench behavior at the micrometer scale within a tape at any location of interest within a coil without requiring a computationally extensive model of the entire coil. This approach also enables the building of more complicated models by hierarchically integrating smaller modular blocks with the same repeatable modeling techniques. Here, the development of the electro–magneto–thermal coil quench model is first presented, followed by its experimental validation. Simulation results and their implications for coil reliability and quench detection and protection are then discussed.**

***Index Terms*—High-aspect-ratio thin layer, multiscale coil model, $REBa_2Cu_3O_{7-\delta}$ (REBCO), 3-D quench modeling.**

I. Introduction

THE significant progress in the commercial development of (RE)$Ba_2Cu_3O_{7-\delta}$ (REBCO, where RE refers to rare earth elements) coated conductors (CCs) has resulted in the pursuit of numerous system applications, including high-field magnets for scientific research and energy storage and magnets for motors and generators, including those for wind turbines [1]–[6]. The long-term success of REBCO magnet-based systems, however, depends on the development of reliable approaches to quench protection, which is essential for ensuring the survival of magnets in the event of a quench. In general, quench protection requires timely quench detection with an effective approach for eliminating false positives, followed by a protective response that prevents conductor degradation. While quench protection is well understood for NbTi- and Nb_3Sn-based superconducting magnets, REBCO CCs and magnets have very slow normal zone propagation velocity (NZPV), rendering quench detection particularly challenging [7]–[17]. Thus, one important goal is to develop REBCO-based magnets that not only are stable, with the ability to tolerate a relatively large disturbance, but also have a sufficient NZPV for effective quench detection and protection.

A typical CC is composed of laminated high-aspect-ratio layers, including a nickel-alloy substrate that provides strength and strain tolerance; thin buffer layers (typically oxides) that chemically isolate the REBCO from the nickel alloy; the superconducting REBCO layer; a silver cap layer that protects the REBCO; and a stabilizer, typically copper, that surrounds and encases the conductor. Descriptions of REBCO CC architectures have been previously detailed [18]–[22].

Variations in the CC geometry or material properties can profoundly affect its quench characteristics, including the NZPV, energy margin, and the time- and spatially varying voltage and temperature within the conductor [7], [8], [12], [23]–[28]. Due to differences in coefficients of thermal expansion (CTEs) of the constituent layers, changes in temperature and temperature gradient can dramatically alter the thermal stresses and strains within the CC during a quench, leading to conductor degradation. A recent study has examined the effects of varying CC material properties on the conductor quench behavior [23]. For example, by using a substrate of higher thermal and electrical conductivity values than the commonly used Hastelloy C276 substrate, one can reduce the NZPV, the peak local temperature, and the spatial and temporal temperature gradients while slowing the rate of voltage rise and increasing the minimum quench energy (MQE). Depending on the quench detection and protection methods, these changes can be favorable or unfavorable. Lower temperature and temperature gradients provide more time for detection and protection, but the slower voltage rise also leads to more difficult detection with traditional voltage or resistance sensing. As alternative detection technologies evolve, for example, optical fiber sensors, detection requirements may also change; in the case of optical fibers, reduced temperature and temperature gradient may reduce the effective sensitivity of the sensor [29]–[32]. More generally, this study showed that relatively small variations in the CC architecture can significantly alter the quench behavior, and thus, the conductor should be designed and optimized in concert with the

Manuscript received January 2, 2012; revised April 18, 2012; accepted April 22, 2012. Date of current version August 28, 2012. This work was supported by the Air Force Research Laboratory. This paper was recommended by Associate Editor M. Noe.

The authors are with the Department of Materials Science and Engineering, North Carolina State University, Raleigh, NC 27695-7907 USA.

Color versions of one or more of the figures in this paper are available online at http://ieeexplore.ieee.org.

Digital Object Identifier 10.1109/TASC.2012.2198647

design optimization of the magnet, including the design of the quench protection system.

Common methods for modeling the quench behavior of superconducting magnets include the use of a variety of modeling techniques, such as analytical equations [25], [26], equivalent network circuits with lumped elements [33]–[35], homogenized coil models [36]–[41], and coils that are homogenized at the conductor level [42]–[46]. A homogenized coil model ignores the distribution of materials within the conductor and the magnet by considering only effective homogenized material properties. A model that homogenizes at the conductor level preserves the turn-to-turn conductor/insulation geometry but includes no details of the internal structure of the conductor. These models are often coupled with electrical circuits to model the dynamic current and voltage changes during the process of quench detection and protection. Due to the homogenization, however, they provide only rough quench information and cannot evaluate phenomena within the conductor itself.

An experimentally validated model of quenching in a REBCO CC tape was previously reported [47]. This conductor model is an accurate micrometer-scale model that uses a mixed-dimensional modeling approach to address the computational challenges of modeling a high-aspect-ratio multilayer system. The model includes all of the thin layers within a CC, including the REBCO layer and thin silver and buffer interlayers, which are addressed with 2-D equations and internal 2-D boundary conditions (BCs). The remaining relatively thick layers, including the stabilizer and the substrate, are modeled with 3-D physics. The interior BCs also couple the 2- and 3-D physics. The model can calculate the temperature and voltages within each layer as a function of location and time during a quench and accurately predicts the quench behavior observed in experiments, including the NZPV and the voltage and temperature profiles. Because each layer is modeled without any averaging of material properties, it is easy to model the effects of variations in architecture on the quench behavior, as reported in [23].

Here, a hierarchical multiscale computationally efficient model of quenching in REBCO magnets is presented. The multiscale model uses the previously reported conductor model as its basic building block. Using the conductor model throughout an entire magnet, however, would be computationally prohibitive; hence, instead, the multiscale magnet model integrates the conductor model with a homogenized model of the entire magnet. Within the homogenized coil framework, one or more localized micrometer-scale multilayer tape modules are embedded at particular locations of interest. The locations of interest can be varied to account for location-dependent effects such as cooling conditions, the dependence of the critical current density on magnetic field and its orientation, or regions where larger heat loads are anticipated. For example, one localized multilayer tape module can be placed at the edge of the coil and another module at the center of the global homogenized coil. The multilayer module models a small section of the coil in detail and is also built using a hierarchical approach by integrating and coupling multiple single-layer CC tape modules that analyze the behavior within each layer of the REBCO CC. The single-layer CC modules are separated by insulation layers that are also physically modeled.

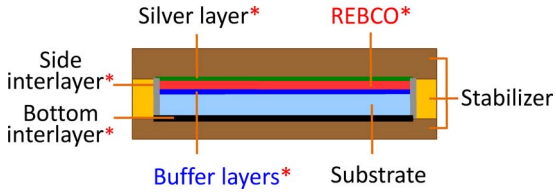

Fig. 1. Cross-sectional schematic of a typical REBCO CC as used in the model [47]. Starred layers are thin layers modeled with 2-D physics; all other layers are modeled in 3-D.

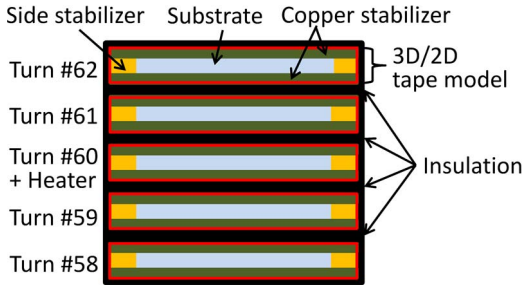

Fig. 2. Schematic showing the cross section of a multilayer tape module composed of five layers of CC.

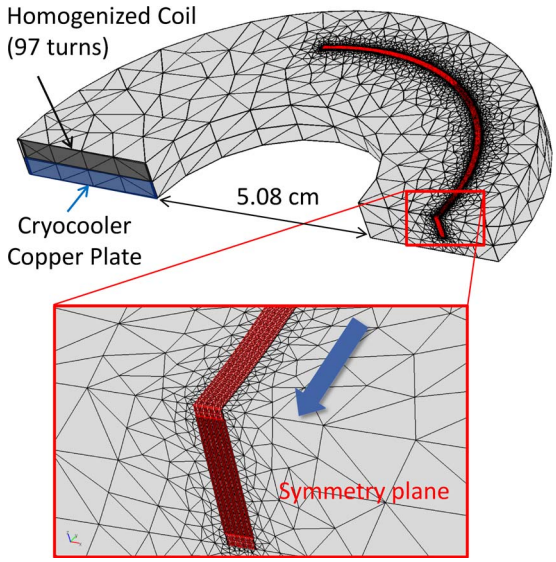

Fig. 3. Multiscale coil model composed of a homogenized coil, a copper plate, and a localized embedded multilayer tape module. The inset shows a section of the multilayer tape module whose cross section is illustrated in Fig. 2. The arrow shows the direction of the current flow in each turn. The current outflow ends of the tapes are located on the symmetry plane. The current inflow ends are located at the other end of the multilayer tape model. Not shown here is the air region, which is a half-rectangle enclosing the half-cylinder coil model, used for the magnetic field calculation.

The hierarchical multiscale approach is illustrated in Figs. 1–3. Fig. 1 illustrates a cross-sectional schematic of a typical CC tape model from [47], which is the fundamental building block used here. These are stacked to create the multilayer modules as shown in Fig. 2. The multilayer modules are then embedded in select locations of an otherwise homogenized coil model as illustrated by the example shown in Fig. 3. By using this multiscale approach, the coil model generates detailed quench properties from the micrometer tape-layer scale to the coil-dimension scale, while ensuring that the coil model

remains computationally manageable. Furthermore, using the single-layer and multilayer tape modules as basic building blocks, more complicated models can be built hierarchically and modularly by applying the same modeling techniques. For example, a pancake coil built from multiple embedded multilayer tape modules can be coupled together to form a complete multisectioned coil entity. In general, all models can be built using the actual dimensions and configurations of the real coils.

II. Multiscale REBCO CC Coil Model

The multiscale coil model uses the same mixed-dimensional modeling approach introduced in [47] to couple multiple single-layer CC tape modules and insulation layers to form a multilayer tape module with the same dimensions and configuration of a real coil. The coil model is implemented using the commercial finite-element multiphysics simulation software COMSOL. A detailed description of the single-layer electro–thermal CC tape model was presented in [47]. Here, some basic equations and modeling techniques from [47] that are essential to the understanding of the electro–magneto–thermal coil model are summarized.

The goal is to investigate quench behavior of a coil carrying a direct transport current. In view of the slow NZPV in REBCO CC-based coils, the slowly varying time-derivative term of the magnetic potential is ignored, thereby decoupling the magnetic and electric potentials in Maxwell equations. The governing electrical and magnetic equations for the 3-D domains are then

$$\nabla \cdot (-\sigma_\alpha(T)\nabla V) = 0 \quad \text{in } \Omega_\alpha \tag{1}$$

$$\mathbf{J} = \sigma_\alpha(T)\mathbf{E} \quad \text{in } \Omega_\alpha \tag{2}$$

$$\mathbf{E} = -\nabla V \quad \text{in } \Omega_\alpha \tag{3}$$

$$\nabla \times \frac{1}{\mu_0}\nabla \times \mathbf{A} = \mathbf{J} \quad \text{in } \Omega_\alpha \tag{4}$$

$$\nabla \times \frac{1}{\mu_0}\nabla \times \mathbf{A} = 0 \quad \text{in } \Omega_{\text{air}}. \tag{5}$$

The magnetic equations (4) and (5) are used only when magnetic field calculation is involved. The externally applied current is input via a normal flux BC imposed on the current input end of the tape model. See [47] for details on the BCs. The thermal equations for the 3-D domains are

$$\rho_\alpha\,(T)\,C_\alpha(T)\frac{\partial T}{\partial t} + \nabla \cdot (-K_\alpha(T)\nabla T) = \mathbf{J}\cdot\mathbf{E} \equiv Q \quad \text{in } \Omega_\alpha \tag{6}$$

where V is the electric potential, T is the absolute temperature, $\mathbf{J}$ is the current density, $\mathbf{E}$ is the electric field, Q is the Joule heating, $\mathbf{A}$ is the magnetic potential, σ_α is the electrical conductivity, ρ_α is the density, C_α is the specific heat capacity, K_α is the thermal conductivity, μ_0 is the permeability, Ω_α is the computational domain, and Ω_{air} is the air region for field computation. Here, $\alpha \in \{\text{cu}, \text{ni}\}$, where "cu" represents the copper stabilizer, and "ni" represents the nickel-alloy substrate.

The high-aspect-ratio thin layers, namely, the REBCO, silver, and buffer layers, are modeled with 2-D physics. On the REBCO layer, the thermal physics is approximated with a 2-D tangential equation and is discretized with 2-D Lagrange finite elements as

$$d_y\rho_y\,(\tilde{T})\,C_y(\tilde{T})\frac{\partial \tilde{T}}{\partial t} - d_y\nabla_t \cdot \left(K_y(\tilde{T})\nabla_t \tilde{T}\right) = d_y Q_y + \frac{K_S}{d_S}\left(T_{\text{cu}}^- - T^+\right) + \frac{K_b}{d_b}\left(T_{\text{ni}}^+ - T^-\right) \quad \text{in } \Omega_y \tag{7}$$

and similarly, the electric physics on the REBCO layer is approximated by a 2-D tangential equation as

$$d_y\nabla_t \cdot \left(-\sigma_y(\tilde{T},\mathbf{B})\nabla_t \tilde{V}\right) = \frac{\sigma_S}{d_S}\left(V_{\text{cu}}^- - V^+\right) + \frac{\sigma_b}{d_b}\left(V_{\text{ni}}^+ - V^-\right) \quad \text{in } \Omega_y \tag{8}$$

where $\tilde{T} = (1/d_y)\int_0^{d_y} T\ dz$, $\tilde{V} = (1/d_y)\int_0^{d_y} V\,dz$, and ∇_t is the 2-D tangential operator, which, in a flat plane, can be written as $\nabla_t = (\partial/\partial x) + (\partial/\partial y)$. The subscripts y, S, and b respectively represent the REBCO, silver, and buffer layers; d_y, d_S, and d_b represent the thicknesses of the REBCO, silver, and buffer layers. In (7), $Q_y = \mathbf{J}_y \cdot \mathbf{E}$ is the Joule heating, where $\mathbf{J}_y = \sigma_y\,(T, \mathbf{B})\ \mathbf{E}$, is the REBCO current density and $\sigma_y(T, \mathbf{B})$ is the temperature- and magnetic-field-dependent electrical conductivity of the REBCO layer (described later). T_{cu}^- and T_{ni}^+ represent the temperatures on the lower surface of the top stabilizer and the upper surface of the substrate, respectively, and V_{cu}^- and V_{ni}^+ are the corresponding potentials. T^+ and T^- are the upper and lower surface temperatures of the REBCO layer, and V^+ and V^- are the corresponding potentials. The upper and lower temperatures and potentials are represented by a set of corrective equations that reproduce the temperature gradient across the thickness of a 3-D REBCO layer and eliminate any otherwise artificial current flowing over the normal zone. They greatly improve the accuracy of the reduced dimensional approximation (see [47]).

The heat transfer in the silver and buffer layers are modeled with internal Neumann BCs, which include normal heat fluxes, surface heat equations, and heat sources. Similarly, the currents flowing across the thicknesses of the silver and buffer layers are approximated by interior normal flux type Neumann BCs. These BCs are imposed on the top copper stabilizer lower surface Γ_{cu}^- and the substrate upper surface Γ_{ni}^+. They also serve as a bridge to couple the 2-D physics modeled by (7) and (8) to the 3-D physics represented by (1)–(3) and (6) (see [47]).

To account for the self-field generated by a single-layer CC tape, both the redistributed current (during current sharing) on the 3-D domains of the tape as calculated by (1)–(3) and the current on the thin REBCO layer as calculated by (8) have to be considered. The field generated in the 3-D and air domains is calculated by (4) and (5), respectively. To simplify the problem formulation and computation, the current on the REBCO layer is approximated as an equivalent 2-D surface current flowing on the interface between the top stabilizer and the substrate (at the place where the REBCO layer is located). The surface current is implemented as an interior surface-current BC [48] as

$$\mathbf{n} \times (\mathbf{H}_{\text{cu}} - \mathbf{H}_{\text{ni}})|_{\{\Gamma_{\text{cu}}^-, \Gamma_{\text{ni}}^+\}} = d_y\,\mathbf{J}_y \tag{9}$$

where $\mathbf{H}_{\rm cu}$ and $\mathbf{H}_{\rm ni}$ are the magnetic fields on the top stabilizer and the substrate, respectively, and $\{\Gamma^-_{\rm cu}, \Gamma^+_{\rm ni}\}$ denotes the identity-pair (COMSOL terminology, see [48] and [49]) connecting the boundaries $\Gamma^-_{\rm cu}$ and $\Gamma^+_{\rm ni}$. By pairing the boundaries $\Gamma^-_{\rm cu}$ and $\Gamma^+_{\rm ni}$ as an identity-pair, the BC (9) is only effective on these two paired boundaries, although the REBCO layer is sandwiched between them. In other words, the magnetic field generated by the REBCO current is not directly calculated by an equivalent 2-D magnetostatic equation on the REBCO layer but is equivalently calculated from a surface current on the interface between the 3-D stabilizer and the substrate. This approach effectively takes into account the self-field generated by the REBCO current and the current redistributed to the 3-D domains during a quench while avoiding the difficulty associated with coupling a 2-D magnetostatic equation to one that is 3-D. Since no real magnetostatic equation is solved on the REBCO layer, however, neither the nonuniform current distribution nor flux jumping in the superconducting REBCO layer as predicted by the Bean model is modeled. This microscopic nonuniform current behavior should not have a significant effect on the quench behavior nor on the generated magnetic field distribution, and the 3-D/2-D mixed-dimensional electro–magneto–thermal tape model is sufficiently accurate for practical modeling of quench behavior in tapes and coils.

To account for the dependence of J_c on temperature and magnetic field [50], J_c is approximated by

$$J_c(T, \mathbf{B}) = J_c(T) f(B, \theta) \tag{10}$$

where $\mathbf{B}$ is the magnetic flux density, and $f(B, \theta)$ is a function that depends on magnitude $B = \|\mathbf{B}\|$ and angle θ. This function is obtained by curve fitting experimental data (for example, see [51]). In (10), the temperature and field are independent of each other. More accurate equations can be used to express J_c as $J_c(T, \mathbf{B}) = g(T, B, \theta)$ for some function g. The simplest form of (10) can be written as

$$J_c(T, \mathbf{B}) = J_c(T) \frac{B_0}{B + B_0} \tag{11}$$

where B_0 is a material-dependent constant, and $J_c(T)$ expresses the temperature dependence as

$$J_c(T) = \begin{cases} J_{\rm co} \left(\frac{T_c - T}{T_c - T_o} \right)^{\beta}, & \text{if } T < T_c \\ 0, & \text{if } T \geq T_c. \end{cases} \tag{12}$$

Here, $J_{\rm co}$ is the critical current density at the operating temperature T_o, T_c is the critical temperature, and β is the power index in the $J - T$ relation. Finally, the electrical conductivity of REBCO is approximated by a nonlinear $E - J$ power law equation, which, when combined with (10), becomes

$$\sigma_y(T, \mathbf{B}) = J_c(T, \mathbf{B}) \frac{\|\mathbf{E}\|^{\frac{1-n}{n}}}{E_c^{\frac{1}{n}}} + \sigma_0 \tag{13}$$

where the critical electric field $E_c = 10^{-4}$ V/m, and n is the $E - J$ power law index. σ_0 is a small constant on the order of 10^{-16} added to ease numerical convergence. Note that the electrical, magnetic, and thermal equations are tightly coupled to each other. Fig. 4 illustrates how the electric, thermal, magnetostatic, and structural mechanics interact and couple to each other. The loose coupling of structural mechanics to the tape/coil model and the analysis of mechanical behavior during a quench will be separately reported.

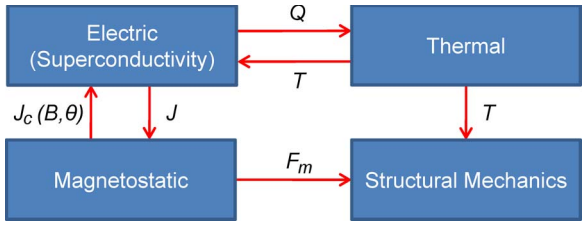

Fig. 4. Coupling relationship between various analysis modes. Here, Q is Joule heating, T is temperature, J is current density, and F_m is magnetic force. In addition, shown is the coupling of structural mechanics, which will be reported elsewhere.

The mutilayer tape module is built by stacking multiple tape models and/or configuring them side-to-side. Regardless of configuration, electrical insulation separates adjacent tapes (Fig. 2 illustrates a stack of tapes). The presence of electrical insulation between adjacent tapes is modeled with the same techniques used for a single tape, as described in [47]. For example, the insulation layers are modeled as two pairs of interior BCs (as identity-pair BCs, similar to the implementations of the silver and buffer layers previously mentioned), i.e., one for the thermal physics and the other for the electric, as

$$\begin{aligned} -K_i \nabla T \cdot \mathbf{n}|_{\Gamma_i} &= \frac{K_{\rm ins}}{d_{\rm ins}} (T_i - T_j) - d_{\rm ins} \rho_{\rm ins}\, C_{\rm ins} \frac{\partial T}{\partial t} \\ &\quad + d_{\rm ins} \nabla_t \cdot (K_{\rm ins}(T) \nabla_t T) \\ -K_j \nabla T \cdot \mathbf{n}|_{\Gamma_j} &= \frac{K_{\rm ins}}{d_{\rm ins}} (T_j - T_i) \end{aligned} \tag{14}$$

$$\begin{aligned} -\sigma_i \nabla V \cdot \mathbf{n}|_{\Gamma_i} &= \frac{\sigma_{\rm ins}}{d_{\rm ins}} (V_i - V_j) \\ -\sigma_j \nabla V \cdot \mathbf{n}|_{\Gamma_j} &= \frac{\sigma_{\rm ins}}{d_{\rm ins}} (V_j - V_i). \end{aligned} \tag{15}$$

Here, the indexes i and j denote tapes i and j between which the insulation layer is inserted. K_i and σ_i are the thermal and electrical conductivity values on tape i; Γ_i is the boundary on the surface of tape i that faces tape j; and $K_{\rm ins}$, $\sigma_{\rm ins}$, and $d_{\rm ins}$ are the thermal and electrical conductivity values and thickness of the insulation. The temperature difference terms on the right-hand sides (RHSs) of (14) are the symmetric normal-directional temperature fluxes flowing across the thickness of the insulation. Similarly, the potential difference terms on the RHSs of (15) are the symmetric normal-directional current fluxes. For insulation with low thermal conductivity in which the in-plane heat transfer is not significant, the surface heat transfer equation (second and third terms) on the RHS of the first equation in (14) can be ignored. If the insulation is thick (on the order of the thicknesses of the 3-D layers of a tape) and thermally conductive, then a 3-D domain is needed to model the insulation and heat transfer. In the case where the insulation

is treated as 2-D BCs as in (14) and (15), since the insulation is generally electrically insulating, there is no current flowing within the insulation. Therefore, the normal current fluxes on the RHS of the BC pair (15) can be set to zero, effectively turning (15) into electrically insulting BCs. In addition, in this case, the tangential magnetic field across the insulation is considered continuous and is enforced on the identity-pair $\{\Gamma_{\rm cu}^{-}, \Gamma_{\rm ni}^{+}\}$ by a field continuity BC as

$$\mathbf{n} \times (\mathbf{H}_i - \mathbf{H}_j)|_{\{\Gamma_i,\, \Gamma_j\}} = \mathbf{0} \tag{16}$$

where $\mathbf{H}_i$ is the magnetic fields on the boundary Γ_i.

Finally, a hierarchical multiscale coil model is built by embedding one or more localized multilayer tape modules within a homogenized coil at locations of interest. Fig. 3 illustrates a multiscale coil model example with one multilayer tape module embedded at the center. In this example, five layers of CC comprise the multilayer tape module, as illustrated in Fig. 2. More layers can be included to improve accuracy and perform longer quench simulations for larger normal zone propagation (with the current-sharing region extended beyond five layers of tape). The coupling between the multilayer tape module and the homogenized coil is implemented with the same techniques used to build the multilayer tape module. The only differences are that, in (14), (15) and (16), one side of the boundary and material properties are from the outermost tape surface of the multilayer tape module, and those on the other side are from the homogenized coil. The outer electrical and thermal BCs of the complete coil can be set according to the cooling configuration.

The magnetic field generated by a coil is calculated by superposing the fields generated by the multilayer module and the homogenized coil. Since all turns carry the same current, all single-layer CCs in a multilayer tape module and the homogenized coil carry the same engineering current density. The total magnetic field is calculated using (8) for the current density on each individual tape, and (4) and (9) for the homogenized coil and (5) for the air region. Externally applied magnetic field can be added as a BC to the air region and coupled to the multilayer tape module through the field-dependent electrical conductivity in (13). The air region (not shown in Fig. 3) is not needed for the electric and thermal physics. More complicated models, such as a multisectioned coil, can be modularly built by repeating the same modeling procedure.

III. Experimental Validation of the Electro–Thermal Tape Model

The 3-D electro–thermal coil model is validated using experimental data previously generated from quench experiments on a single pancake REBCO coil [8]. The coil, which is illustrated in Fig. 5, consists of 97 turns of CC with an inner diameter of 5.08 cm and is cooled at the bottom via a copper plate attached to the cold finger of a cryocooler. The rest of the coil is adiabatic with an initial operating temperature of 50 K. The CC is 4.8 mm wide and includes a 52-μm-thick Cu stabilizer on the top and bottom, which is bonded to the CC via solder. More details regarding the REBCO CC are published in [22]. The CC is wrapped by 50-μm-thick paper insulation.

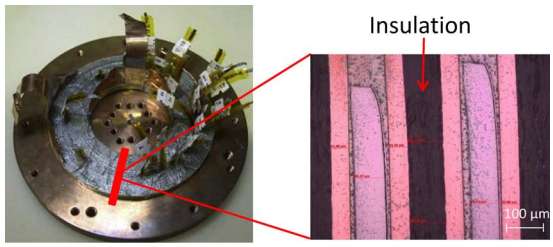

Fig. 5. Single pancake coil used in the quench experiments. The inset shows a cutout section of the coil as viewed in an optical microscope to measure the average thicknesses of the composing layers.

The multiscale coil model is built with the same dimensions and configuration as the experimental coil, as illustrated in Fig. 3. Five layers of CC comprise the embedded localized multilayer tape module, corresponding to turns #58–#62 of the experimental coil, as schematically shown in Fig. 2. The average thicknesses and widths of the constituent layers of the CC and insulation are determined from a cutout section of the coil shown in Fig. 5. Area fractions of the constituent layers of the coil, as derived from the measured dimensions, are used in the equivalent electrical/thermal series [see Fig. 6(a)] and parallel circuits [see Fig. 6(b)] to estimate the effective transverse and longitudinal electrical/thermal conductivity values of the homogenized coil. Effective specific heat of the composite coil is calculated based on area fractions of the constituent materials. Taking advantage of symmetrical/asymmetrical quench properties across the center of the heater, only half of the coil, including the heater, is modeled. Similar to the quench heater implemented in the experimental coil, the half-length heater (25 mm long, 2 mm wide, and 0.02 mm thick) is embedded between turns #59 and #60 (see Fig. 2), starting from the symmetry edge (on the symmetry plane shown in Fig. 3). Current flows from the current inflow end, which is located at the end of the multilayer tape module inside the homogenized coil, to the current outflow end, which is located on the symmetry plane, as illustrated in Fig. 3.

Figs. 7 and 8 compare the longitudinal (parallel to the direction of current flow) and transverse (radial) NZPVs obtained from simulations (solid line) and experiments (dashed line) at 50 K for operating current density (J_a) ranging from 50% to 90% J_c. In each simulation, the same transport current as in the corresponding experiment is used. For example, in the $J_a = 70\%\ J_c$ case, the transport current is 162 A. In this case, the current-sharing temperature $T_{\rm cs} = 61.3$ K. Some of the unknown material properties, such as the electrical and thermal properties of the solder and paper-type insulation, are estimated or parameterized. All simulation cases are quenched with the same quench energy (QE) reported in [8]. The computational MQEs of the multiscale coil model are not determined, but, in general, they are smaller than those experimentally determined because the heater in the model is in perfect contact with the CC, whereas in the experimental coil, there are large nonuniform gaps between the heater and the turns. The NZPVs are computationally determined using the same criteria used experimentally. The longitudinal NZPV is calculated as the distance between two voltage taps (10 mm) divided by the time delay (Δt, see Fig. 9) between $V_{60\_3.5-2.5}$ reaching

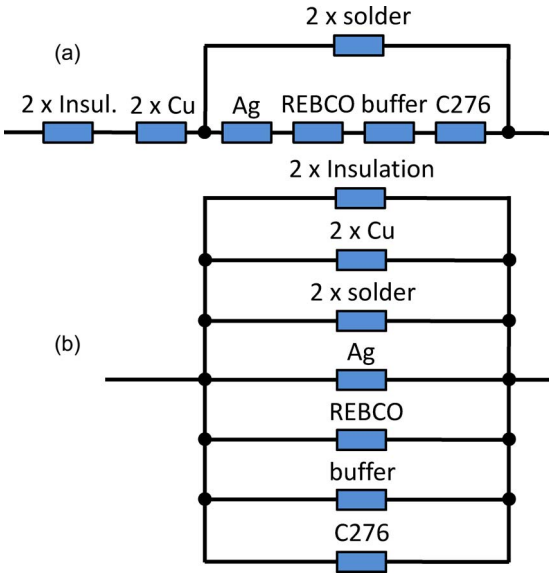

Fig. 6. Equivalent electrical/thermal circuits used to calculate (a) the effective transverse and (b) the effective longitudinal electrical and thermal conductivity values of the homogenized coil.

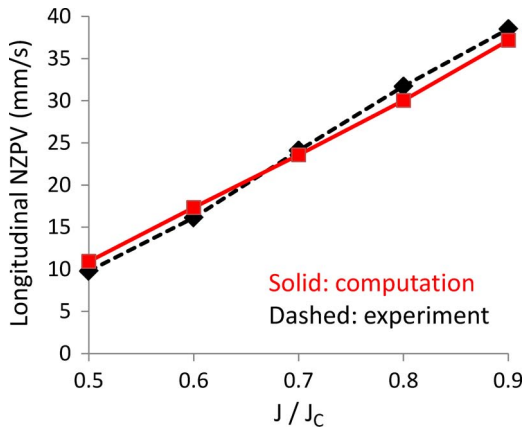

Fig. 7. Comparison of the computational and experimental results of the longitudinal NZPV along the center turn (turn #60). The initial operating temperature is 50 K. All differences are less than 11%.

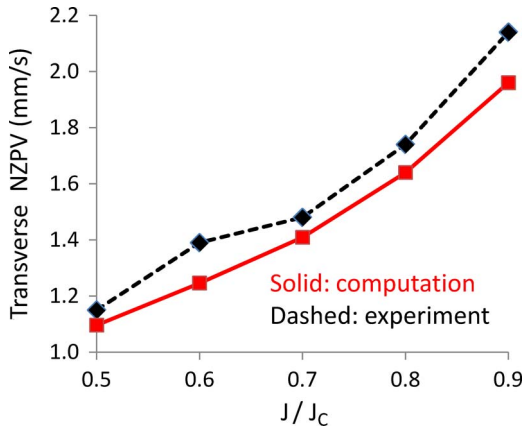

Fig. 8. Comparison of the computational and experimental results for the transverse NZPV. The initial operating temperature is 50 K. All differences are less than 10%.

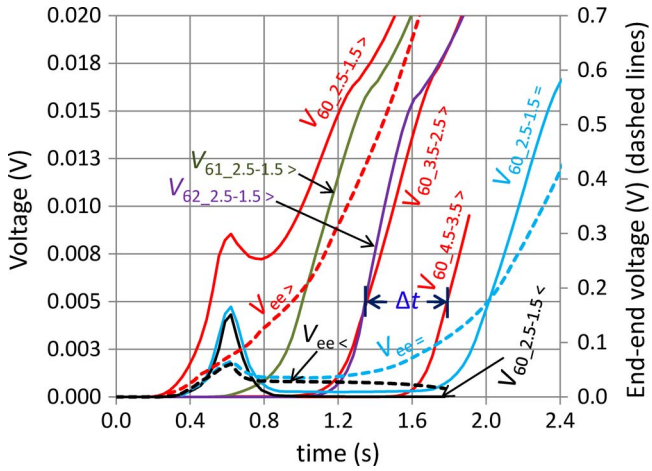

Fig. 9. Voltage versus time during a quench. $V_{60\_2.5-1.5}$ denotes the voltage difference between the voltage taps located at $l = 1.5$ cm and $l = 2.5$ cm on turn #60, where l is the arc length along the tape measured from the current outflow end. V_{ee} (dashed line) is the end-to-end (terminal) voltage, calculated as the sum of all the voltage differences between the current inflow end and the current outflow end from turn #58 to turn #62. The additional subscripts, i.e., ">", "=" and "<," denote that the voltage curve is obtained from a simulation for which the input energy, which is stopped at $t = 0.6$ s, is larger than, equal to, and smaller than the MQE, respectively.

5 mV and $V_{60\_4.5-3.5}$ reaching 5 mV.[1] The transverse NZPV is calculated by dividing the average thickness across a tape-insulation layer (0.41 mm) by the time delay between $2V_{61\_0.5}$ and $2V_{62\_0.5}$, when both have reached 5 mV. All errors (or differences between the computational and experimental results) in the longitudinal NZPVs shown in Fig. 7 are $< 11\%$; for the transverse NZPVs shown in Fig. 8, the errors/differences are $< 10\%$. These errors/differences are primarily attributed to inhomogeneities in the CC used in the experimental coil and in the coil winding itself, as discussed in [8], and also to uncertainties in some of the material properties.

IV. Simulation Results

This section presents some of the quench details captured from the same $J_a = 70\%\ J_c$ case validation simulation described in the previous section. These results also demonstrate the multiscale modeling capabilities of the multiscale coil model.

Fig. 9 plots the voltage versus time at locations on turns #60, #61, and #62. In addition, shown is the end-to-end voltage (V_{ee}) calculated as the sum of all single-turn end-to-end voltages (between the current inflow and outflow ends) obtained from turns #58–#62. As long as the current-sharing region ($T_{cs} >= 61.3$ K) is confined to the multilayer tape volume, V_{ee} represents the end-to-end (terminal) resistive voltage across the entire coil. When the current-sharing region extends beyond the multilayer tape module, however, V_{ee} calculated in this manner would underestimate the actual end-to-end voltage in the coil.

[1]The first number of the subscript refers to the turn number within the coil, and the second number refers to the location of the voltage taps. Thus, for example, $V_{60\_3.5-2.5}$ is the voltage difference between the voltage taps located at $l = 3.5$ cm and $l = 2.5$ cm on turn #60, where l is the arc length along the tape measured from the current outflow end on the symmetry plane.

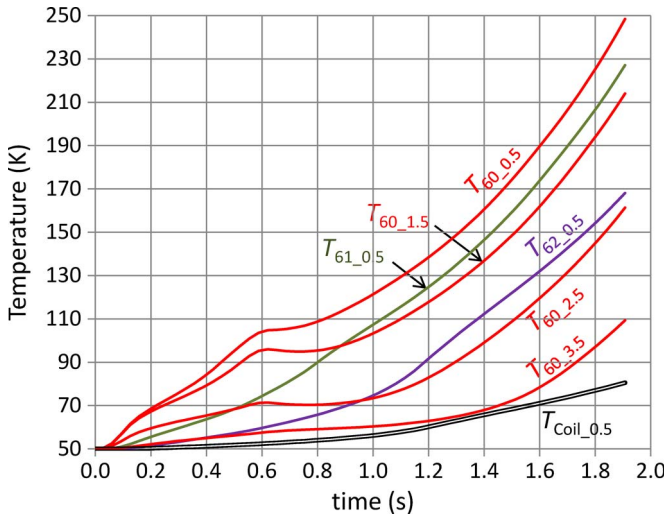

Fig. 10. Temperature versus time during a quench for the QE > MQE case. $T_{60\_0.5}$ denotes the temperature measured on turn #60 at arc length $l = 0.5$ cm, which is measured along the tape from the current outflow end. $T_{\rm coil}$ (bold line) is the temperature taken in the homogenized coil in the vicinity of turn #62, 0.5 cm from the symmetry plane. Note that the QE is stopped at $t = 0.6$ s.

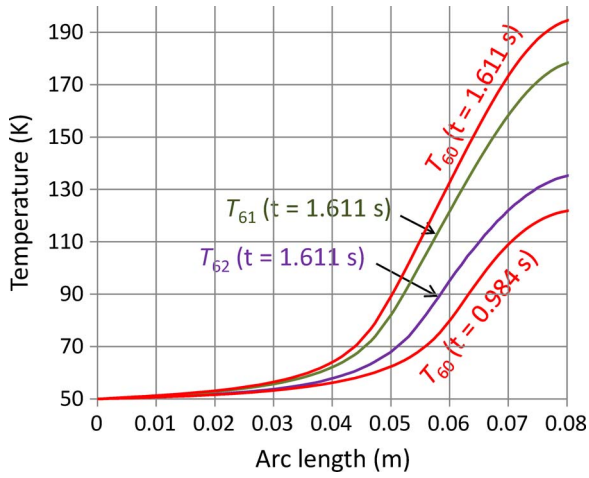

Fig. 11. Temperature versus location for fixed times during a quench for the QE > MQE case. T_{60} ($t = 1.611$ s) and T_{60} ($t = 0.984$ s) are the temperatures at the top Cu surface of turn #60 measured along the arc length (here, zero being at the current inflow end).

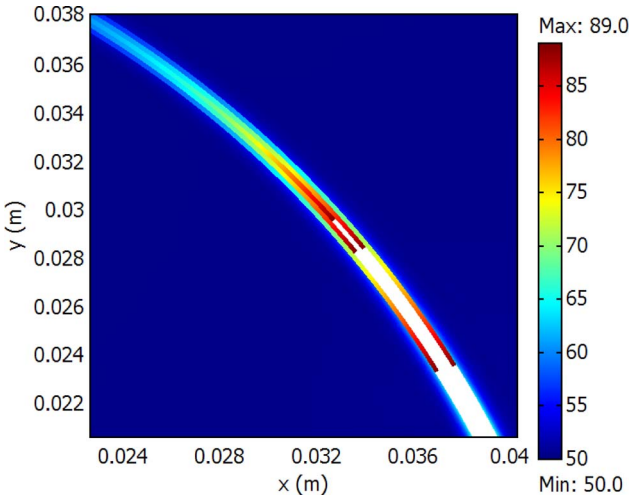

Fig. 12. Snapshot of the temperature distribution for the QE > MQE case, including turns #58–#62 and the homogenized coil, at $t = 1.611$ s. The white portion within the coil denotes the area where $T > T_c = 89$ K. Note that for this simulation, $T_{\rm cs} = 61.3$ K. The center turn, i.e., turn #60, has the fastest normal zone propagation, followed by turns #59 and #61, and then turns #58 and #62. The homogenized portion of the coil is not yet normal.

For example, for the QE > MQE case, when $t >= 1.23$ s, the temperature on the homogenized coil near the vicinity of the multilayer tape module is greater than $T_{\rm cs}$ (see Fig. 10), and as a result, for $t >= 1.23$ s, $V_{\rm ee>}$ shown in Fig. 9 underestimates the end-to-end voltage, here the subscript ">" (see Fig. 9 and its caption for other similar notations) denotes that the voltage curve is obtained from the QE > MQE case simulation. Therefore, to calculate the end-to-end voltage more accurately for a quench in which the quench propagation volume expands beyond the multilayer tape volume, a longer multilayer tape module, or one consisting more than five turns, is needed.

Fig. 10 plots the temperature versus time at fixed locations within the embedded multilayer tape module for QE > MQE. $T_{60\_0.5}$ denotes the temperature at $l = 0.5$ cm on turn #60. In addition, shown is the temperature $T_{\rm coil\_0.5}$ on the homogenized coil measured in the vicinity of the outer layer of turn #62 at a height of 0.5 cm from the symmetry plane. Note that the QE is stopped at $t = 0.6$ s. Large temperature differences between neighboring turns and along a turn are seen. For example, at $t = 1.6$ s, the temperature difference between turns #60 and #62 at $l = 0.5$ cm is about 60 K, and the temperature difference along turn #60 between $l = 0.5$ cm and $l = 2.5$ cm is about 70 K. These large temperature gradients are also shown in Fig. 11, which replots the temperature results as a function of location in terms of the arc length measured from the current inflow end on the top Cu surface along turns #60–#62 at $t = 1.611$ s and $t = 0.984$ s.

Fig. 12 shows a snapshot of the temperature distribution on the top surface of the coil at $t = 1.611$ s for the same QE > MQE case in Fig. 10. The white portion inside the coil denotes to the area where $T > T_c = 89$ K. Recall that $T_{\rm cs} = 61.3$ K; hence, the normal zone is clearly seen. The center turn (turn #60) has the longest normal section since quench began on this layer; the next longest normal zones are on turns #59 and #61, followed by turns #58 and #62, illustrating the effect of low thermal conductivity in the insulation layer and the anticipated symmetry from the simulation. The temperature in the homogenized region of the coil is between 50 and 65 K, and thus, current sharing has begun. The longitudinal NZPV on turn #60 is 23.04 mm/s and about 24.30 mm/s on turns #58, #59, #61, and #62. The NZPV on the center turn #60 is slower than the adjacent turns because there are two cold turns adjacent to the quench front of turn #60. In contrast, on each of the other turns, there is one cold turn and one hot turn, which are heated by transverse heat propagation.

Fig. 13 illustrates the radial temperature profile at a height of 1.5 cm from the symmetry plane at $t = 1.611$ s, giving an alternate view of the temperature distribution depicted in Fig. 12. Large turn-to-turn temperature drops are observed across the insulation layers, which are modeled as internal BCs and, thus, have zero thicknesses. These temperature drops

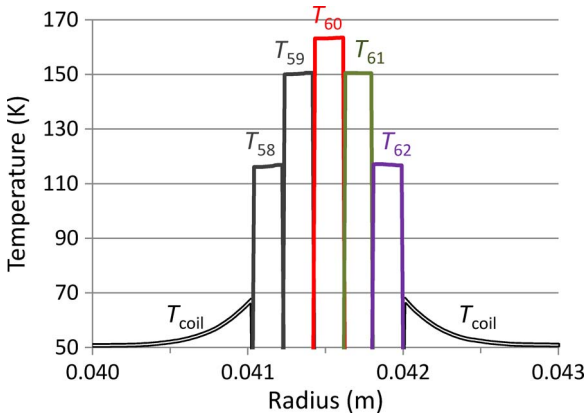

Fig. 13. Radial temperature profile at 1.5 cm from the symmetry plane and $t = 1.611$ s. This corresponds to Fig. 12. Temperature gradients exist across the insulation between adjacent turns. The temperature on the homogenized coil is the average temperature.

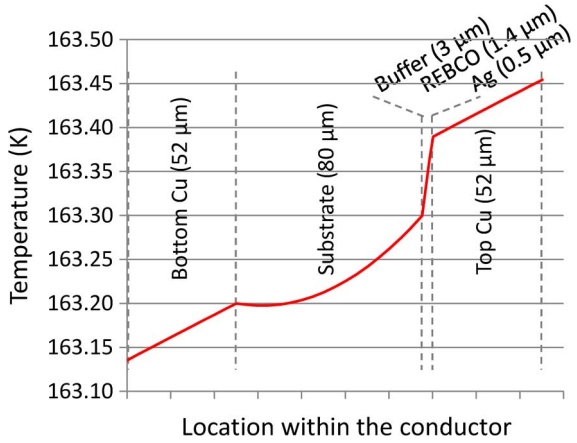

Fig. 14. Localized temperature profile within turn #60 of the multilayer tape module at $t = 1.611$ s and arc length $l = 1.5$ cm, which is measured along the tape from the current outflow end. This corresponds to Fig. 13. Note that there is a temperature gradient across the Ag-REBCO-buffer composite layer whose thickness is exaggerated here for illustration.

across the turns are also shown in Figs. 10 and 11. Note that the temperatures at arc length $l = 0.5$ cm and $t = 1.611$ s in Fig. 10 are higher than those in Fig. 13 because they are observed at locations closer to the peak temperature zone at the center of the heater on the symmetry plane.

Corresponding to Fig. 13, Fig. 14 illustrates the local micrometer-scale temperature profile across the radial cross section of turn #60 at arc length $l = 1.5$ cm and $t = 1.611$ s. There is a large temperature gradient across the Ag-REBCO-buffer composite layer, ~18 K/mm. Note that the thickness of this layer is exaggerated in Fig. 14 for illustration.

V. Discussion

Figs. 9 and 10 give a clear picture of the relationship between the end-to-end voltages V_{ee}'s and the local voltages such as $V_{60\_2.5-1.5}$ and the temperatures such as $T_{60\_0.5}$. Local voltages and temperatures measured from a distributed allocation of taps are often used in single tape experiments to measure quench propagation quantities such as NZPV. In a coil, however, it is more common to use end-to-end voltages across coil subsections. Knowing the local details, however, can be very important in the development of more effective detection/protection systems based on voltage sensing. For example, consider a simple approach based upon a safe maximum hot-spot temperature of 190 K. Suppose the heat energy in the QE > MQE case is the maximum possible disturbance energy, then according to Fig. 10, $T_{60\_0.5}$, which is close to the peak temperature (at the center of the heater) for the QE > MQE case, reaches 190 K at $t = 1.6$ s. This restricts the total detection and protection time to be less than 1.6 s. In Fig. 9, $V_{ee>}$ reaches about 0.68 V at $t = 1.6$ s. Thus, the upper bound for the triggering detection voltage must be well below 0.68 V. The lower bound triggering voltage, however, is harder to determine without details from local voltages. The lower bound must be set sufficiently low to give fast detection but not too low to trigger the protection system due to a false positive relative to the quench threshold detection or a low signal-to-noise ratio in the voltage signal. For example, one cannot get guidance from $V_{ee>}$ to derive the lower bound voltage. One would consider using $V_{ee<}$ in the case for which the QE does not result in a quench and, thus, set the lower bound triggering voltage slightly higher than 0.06 V, which is the peak of $V_{ee<}$ at $t = 0.6$ s. In this case, the magnet will be unnecessarily shut down because further elaboration from QE experiments or simulations will show from $V_{ee=}$ in the QE = MQE case that a quench happens at an end-to-end voltage much higher than 0.06 V. However, one can use the quench detection criterion commonly applied on local voltage taps to derive the lower bound end-to-end triggering voltage. Using $V_{60\_2.5-1.5=}$ (also for the QE = MQE case) as a reference, the 5-mV criterion occurs on $V_{60\_2.5-1.5=}$ at about $t = 2.0$ s. The corresponding $V_{ee=}$ at $t = 2.0$ s is found to be 0.17 V. Thus, the triggering voltage for the protection system would be set at $0.17\ \text{V} < V_{ee} \ll 0.68$ V.

From the temperature data in Fig. 10, $\partial T/\partial t$ at all locations increases with time. One can see from the temperatures T_{60} $(t = 0.984$ s) and T_{60} $(t = 1.611$ s) in Fig. 11 that $\partial T/\partial l$, where l is the arc length, also increases with time. Thus, the normal zone grows sufficiently slow that the local temperature quickly rises, and hot-spot identification is important for quench detection and protection. These larger temperature gradients may be useful in the development of quench detection systems based on sensing methods other than end-to-end voltage measurements, such as optical fiber sensors [29]–[32]. In this case, large temperature gradients may result in easier and more sensitive detection.

Due to the differences in the CTEs of the constituent materials in a CC and coil, the high temperature and large temperature gradients observed in Figs. 10 and 11, and the temperature gaps across the insulation layers illustrated in Figs. 12 and 13, can create large thermal stresses and strains within the CC, insulation, and coil structure [45]. In addition, simulations [47] show that due to the low thermal conductivity values of the REBCO and buffer layers, the temperature gradient across the Ag-REBCO-buffer composite layer, as shown in Fig. 14, can become very large if the temperature difference on the two outermost surfaces of the tape is large. This can happen, for example, if a quench occurs on a tape located at the coil boundary, which is strongly cooled. A large temperature gradient

across the Ag-REBCO-buffer layer can create large interfacial thermal stresses/strains and increase the risk of degradation due to delamination or cracking [52], [53].

VI. Conclusion

The development of an effective quench protection system for REBCO-based magnets relies on the subtleties of the quench behavior at the micrometer scale within a framework of the behavior of the entire magnet. To facilitate thorough modeling of the quench behavior, a multiscale electro–magneto–thermal coil model is built using an experimentally validated multiscale modular modeling approach. The multiscale coil model provides dynamic quench properties at every length scale of interest, ranging from the local micrometer scale within an individual turn of conductor to the macroscopic behavior of the coil. This has the potential to facilitate magnet optimization as well.

The multiscale electro–thermal coil model is validated against experimental data and is shown to be sufficiently accurate for practical application. Local and global temperature and voltage profiles obtained from simulations reveal useful information for setting quench detection criteria. Simulations also show that large temperature gradients can occur across the constituent layers of a conductor and across the insulation layers in the vicinity of the normal zone. These gradients create thermal stresses/strains that may affect coil performance and reliability.

Acknowledgment

The authors would like to thank H. Song for helpful discussions regarding the experimental approach and results found in [8].

References

[1] G. Snitchler, B. Gamble, and S. S. Kalsi, "The performance of a 5 MW high temperature superconductor ship propulsion motor," *IEEE Trans. Appl. Supercond.*, vol. 15, no. 2, pp. 2206–2209, Jun. 2005.

[2] J. Schwartz, "High temperature superconductors for accelerator magnets," in *Proc. Workshop Accel. Magnet Des. Optim.*, 2006, pp. 56–60.

[3] J. Schwartz, T. Effio, X. Liu, Q. V. Le, A. L. Mbaruku, H. J. Schneider-Muntau, T. Shen, H. Song, U. P. Trociewitz, X. Wang, and H. W. Weijers, "High field superconducting solenoids via high temperature superconductors," *IEEE Trans. Appl. Supercond.*, vol. 18, no. 2, pp. 70–81, Jun. 2008.

[4] A. B. Abrahamsen, N. Mijatovic, E. Seiler, T. Zirngibl, C. Trholt, P. B. Nrgård, N. F. Pedersen, N. H. Andersen, and J. stergård, "Superconducting wind turbine generators," *Supercond. Sci. Technol.*, vol. 23, no. 3, p. 034019, Mar. 2010.

[5] D. U. Gubser, "Superconducting motors and generators for naval applications," *Physica C*, vol. 392–396, pp. 1192–1195, Oct. 2003.

[6] U. P. Trociewitz, M. Dalban-Canassy, M. Hannion, D. K. Hilton, J. Jaroszynski, P. Noyes, Y. Viouchkov, H. W. Weijers, and D. C. Larbalestier, "35.4 T field generated using a layer-wound superconducting coil made of (RE)$Ba_2Cu_3O_{7-x}$ (RE = rare earth) coated conductor," *Appl. Phys. Lett.*, vol. 99, no. 20, p. 205506, Nov. 2011.

[7] R. C. Duckworth, J. W. Lue, D. F. Lee, R. Grabovickic, and M. J. Gouge, "The role of nickel substrates in the quench dynamics of silver coated YBCO tapes," *IEEE Trans. Appl. Supercond.*, vol. 13, no. 2, pp. 1768–1771, Jun. 2003.

[8] H. Song, K. Gagnon, and J. Schwartz, "Quench behavior of conduction-cooled $YBa_2Cu_3O_{7-\delta}$ coated-conductor pancake coils stabilized with brass and copper," *Supercond. Sci. Technol.*, vol. 23, no. 6, p. 065021, Jun. 2010.

[9] X. Wang, U. P. Trociewitz, and J. Schwartz, "Near-adiabatic quench experiments on short $YBa_2Cu_3O_{7-\delta}$ coated conductors," *J. Appl. Phys.*, vol. 101, no. 5, p. 053904, Mar. 2007.

[10] X. Wang, U. P. Trociewitz, and J. Schwartz, "Critical current degradation of short $YBa_2Cu_3O_{7-\delta}$ coated conductor due to an unprotected quench," *Supercond. Sci. Technol.*, vol. 24, no. 3, p. 035006, Mar. 2011.

[11] X. R. Wang, A. R. Caruso, M. Breschi, G. Zhang, U. P. Trociewitz, H. W. Weijers, and J. Schwartz, "Normal zone initiation and propagation in Y–Ba–Cu–O coated conductors with Cu stabilizer," *IEEE Trans. Appl. Supercond.*, vol. 15, no. 2, pp. 2586–2589, Jun. 2005.

[12] X. R. Wang, U. P. Trociewitz, and J. Schwartz, "Self-field quench behavior of $YBa_2Cu_3O_{7-\delta}$ coated conductors with different stabilizers," *Supercond. Sci. Technol.*, vol. 22, no. 8, p. 085005, Aug. 2009.

[13] F. Trillaud, A. Caruso, J. Barrow, B. Trociewitz, U. P. Trociewitz, H. W. Weijers, and J. Schwartz, "Normal zone generation and propagation in $YBa_2Cu_3O_{7-\delta}$ coated conductors initialized by localized pulsed disturbances," *Adv. Cryogenic Eng. Mater.*, vol. 711, no. 1, pp. 852–859, 2004.

[14] F. Trillaud, H. Palanki, U. P Trociewitz, S. H. Thompson, H. W. Weijers, and J. Schwartz, "Normal zone propagation experiments on HTS composite conductors," *Cryogenics*, vol. 43, no. 3–5, pp. 271–279, Mar.–May 2003.

[15] H. H. Song and J. Schwartz, "Stability and quench behavior of $YBa_2Cu_3O_{7-x}$ coated conductor at 4.2 K, self-field," *IEEE Trans. Appl. Supercond.*, vol. 19, no. 5, pp. 3735–3743, Oct. 2009.

[16] A. Ishiyama, M. Yanai, T. Morisaki, H. Ueda, Y. Shiohara, T. Izumi, Y. Iijima, and T. Saitoh, "Normal transition and propagation characteristics of YBCO tape," *IEEE Trans. Appl. Supercond.*, vol. 15, no. 2, pp. 1659–1662, Jun. 2005.

[17] R. Grabovickic, J. W. Lue, M .J. Gouge, J. A. Demko, and R. C. Duckworth, "Measurements of temperature dependence of the stability and quench propagation of a 20-cm-long RABiTS Y–Ba–Cu–O tape," *IEEE Trans. Appl. Supercond.*, vol. 13, no. 2, pp. 1726–1730, Jun. 2003.

[18] D. W. Hazelton and V. Selvamanickam, "SuperPower's YBCO coated high-temperature superconducting (HTS) wire and magnet applications," *Proc. IEEE*, vol. 97, no. 11, pp. 1831–1836, Nov. 2009.

[19] T. G. Holesinger, L. Civale, B. Maiorov, D. M. Feldmann, J. Y. Coulter, D. J. Miller, V. A. Maroni, Z. Chen, D. C. Larbalestier, R. Feenstra, X. Li, Y. Huang, T. Kodenkandath, W. Zhang, M. W. Rupich, and A. P. Malozemoff, "Progress in nanoengineered microstructures for tunable high-current, high-temperature superconducting wires," *Adv. Mater.*, vol. 20, no. 3, pp. 391–407, Feb 2008.

[20] V. Selvamanickam, Y. Chen, X. Xiong, Y. Y. Xie, M. Martchevski, A. Rar, Y. Qiao, R. M. Schmidt, A. Knoll, K.P. Lenseth, and C. S. Weber, "High performance 2G wires: From R&D to pilot-scale manufacturing," *IEEE Trans. Appl. Supercond.*, vol. 19, no. 3, pp. 3225–3230, Jun. 2009.

[21] V. Selvamanickam, A. Guevara, Y. Zhang, I. Kesgin, Y. Xie, G. Carota, Y. Chen, J. Dackow, Y. Zhang, Y. Zuev, C. Cantoni, A. Goyal, J. Coulter, and L. Civale, "Enhanced and uniform in-field performance in long (Gd, Y)–Ba–Cu–O tapes with zirconium doping fabricated by metal–organic chemical vapor deposition," *Supercond. Sci. Technol.*, vol. 23, no. 1, p. 014014, Jan. 2010.

[22] A. P. Malozemoff, S. Fleshler, M. Rupich, C. Thieme, X. Li, W. Zhang, A. Otto, J. Maguire, D. Folts, J. Yuan, H.-P. Kraemer, W. Schmidt, M. Wohlfart, and H.-W. Neumueller, "Progress in high temperature superconductor coated conductors and their applications," *Supercond. Sci. Technol.*, vol. 21, no. 3, p. 034005, Mar. 2008.

[23] W. K. Chan and J. Schwartz, "Three-dimensional micrometer-scale modeling of quenching in high-aspect-ratio $YBa_2Cu_3O_{7-\delta}$ coated conductor tapes; Part II: Influence of geometric and material properties and implications for conductor engineering and magnet design," *IEEE Trans. Appl. Supercond.*, vol. 21, no. 6, pp. 3628–3634, Dec. 2011.

[24] G. A. Levin, P. N. Barnes, J. P. Rodriguez, J. A. Connors, and J. S. Bulmer, "Stability and normal zone propagation speed in YBCO coated conductors with increased interfacial resistance," *IEEE Trans. Appl. Supercond.*, vol. 19, no. 3, pp. 2504–2507, Jun. 2009.

[25] G. A. Levin, W. A. Jones, K. A. Novak, and P. N. Barnes, "The effects of superconductor-stabilizer interfacial resistance on quenching of a pancake coil made out of coated conductor," *Supercond. Sci. Technol.*, vol. 24, no. 3, p. 035015, Mar. 2011.

[26] A. Ishiyama, H. Ueda, T. Ando, H. Naka, S. Bamba, and Y. Shiohara, "A criterion for determining stabilizer thickness of YBCO coated conductors based on coil protection," *IEEE Trans. Appl. Supercond.*, vol. 17, no. 2, pp. 2430–2433, Jun. 2007.

[27] R. G. Mints, T. Ogitsu, and A. Devred, "Quench propagation velocity for highly stabilized conductors," *Cryogenics*, vol. 33, no. 4, pp. 449–453, 1993.
[28] M. Polak, P. N. Barnes, and G. A. Levin, "YBCO/Ag boundary resistivity in YBCO tapes with metallic substrates," *Supercond. Sci. Technol.*, vol. 19, no. 8, pp. 817–820, Aug. 2006.
[29] J. H. Schultz, "Protection of superconducting magnets," *IEEE Trans. Appl. Supercond.*, vol. 12, no. 1, pp. 1390–1395, Mar. 2002.
[30] J. Schwartz, R. P. Johnson, S. A. Kahn, and M. Kuchnir, "Multi-purpose fiber optic sensors for HTS magnets," presented at the 11th European Particle Accelerator Conf., Genoa, Italy, 2008.
[31] M. Turenne, R. Johnson, F. Hunte, J. Schwartz, and H. Song, "Multi-purpose fiber optic sensors for high temperature superconductor magnets," in *Proc. Particle Accelerator Conf.*, Vancouver, BC, Canada, 2009.
[32] F. Hunte, H. Song, J. Schwartz, R. Johnson, and M. Turenne, "Fiber Bragg optical sensors for YBCO applications," in *Proc. Particle Accelerator Conf.*, Vancouver, Canada, 2009.
[33] A. M. Miri, C. Sihler, M. Droll, and A. Ulbricht, "Modeling the transient behavior of a large superconducting coil subjected to high voltage pulses," in *Proc. Int. Conf. Power Syst. Transients*, Lisbon, Portugal, 1995, pp. 57–62.
[34] A. M. Miri, S. Fink, and W. H. Fietz, "Transient behaviour of superconducting magnet systems of fusion reactor ITER during safety discharge," *Modelling Simul. Eng.*, vol. 2008, p. 359210, 2008.
[35] D. Bocian, B. Dehning, and A. Siemko, "Modeling of quench limit for steady state heat deposits in LHC magnets," *IEEE Trans. Appl. Supercond.*, vol. 18, no. 2, pp. 112–115, Jun. 2008.
[36] N. Schwerg, B. Auchmann, and S. Russenschuck, "Quench simulation in an integrated design environment for superconducting magnets," *IEEE Trans. Magn.*, vol. 44, no. 6, pp. 934–937, Jun. 2008.
[37] Z. P. Zhao and Y. Iwasa, "Normal zone propagation in adiabatic superconducting magnets. Part 1: Normal zone propagation velocity in superconducting composites," *Cryogenics*, vol. 31, no. 9, pp. 817–825, Sep. 1991.
[38] V. Picaud, P. Hiebel, and J.-M. Kauffmann, "Superconducting coils quench simulation, the Wilson's method revisited," *IEEE Trans. Magn.*, vol. 38, no. 2, pp. 1253–1256, Mar. 2002.
[39] K. Koyanagi, M. Ono, S. Hanai, K. Watanabe, S. Awaji, T. Hamajima, T. Kiyoshi, and H. Kumakura, "Design of a 30 T superconducting magnet using a coated conductor insert," *IEEE Trans. Appl. Supercond.*, vol. 19, no. 3, pp. 1617–1620, Jun. 2009.
[40] M. Ristic, J. V. M. McGinley, and F. Lorenzoni, "Numerical study of quench protection schemes for a MgB_2 superconducting magnet," *IEEE Trans. Appl. Supercond.*, vol. 21, no. 5, pp. 3501–3508, Oct. 2011.
[41] L. Wang, H. Pan, X. L. Guo, H. Wu, S. X. Zheng, and M. A. Green, "Study on the mechanical instability of MICE coupling magnets," *IEEE Trans. Appl. Supercond.*, vol. 21, no. 3, pp. 2363–2366, Jun. 2011.
[42] K. Higashikawa, T. Kiss, M. Inoue, S. Awaji, K. Watanabe, H. Fukushima, Y. Yamada, and Y. Shiohara, "Significant reduction in volume, stored energy and magnetization loss of high-field magnet coil based on the improvement of critical current characteristics in GdBCO coated conductor," *Phys. C-Supercond. Appl.*, vol. 469, no. 15, pp. 1776–1780, Aug.–Oct. 2009.
[43] A. Stenvall, R. Mikkonen, and P. Kovac, "Relation between transverse and longitudinal normal zone propagation velocities in impregnated MgB_2 windings," *IEEE Trans. Appl. Supercond.*, vol. 19, no. 3, pp. 2403–2406, Jun. 2009.
[44] X. Du, M. Jin, Z. Zhang, Z. Xu, L. Ye, D. Zhang, X. Li, G. Zhang, and L. Xiao, "Numerical analysis on the quench process and protection of conduction cooled MgB_2 magnet," *IEEE Trans. Appl. Supercond.*, vol. 20, no. 3, pp. 2102–2106, Jun. 2010.
[45] P. Ferracin, S. Caspi, L. Chiesa, S. A. Gourlay, R. R. Hafalia, L. Imbasciati, A. F. Lietzke, G. Sabbi, and R. M. Scanlan, "Thermal, electrical and mechanical response in Nb_3Sn superconducting coils," *IEEE Trans. Appl. Supercond.*, vol. 14, no. 2, pp. 361–364, Jun. 2004.
[46] A. Ishiyama, H. Matsumura, W. Takita, and Y. Iwasa, "Quench propagation analysis in adiabatic superconducting windings," *IEEE Trans. Magn.*, vol. 27, no. 2, pp. 2092–2095, Mar. 1991.
[47] W. K. Chan, P. J. Masson, C. Luongo, and J. Schwartz, "Three-dimensional micrometer-scale modeling of quenching in high aspect ratio $YBa_2Cu_3O_{7-\delta}$ coated conductor tapes. Part I: Model development and validation," *IEEE Trans. Appl. Supercond.*, vol. 20, no. 6, pp. 2370–2380, Dec. 2010.
[48] COMSOL AC/DC Module User's Guide, version 3.5a or newer.
[49] COMSOL Multiphysics User's Guide, version 3.5a or newer.
[50] T. Kiss, M. Inoue, T. Kuga, M. Ishimaru, S. Egashira, S. Irie, T. Ohta, K. Imamura, M. Yasunaga, M. Takeo, T. Matsushita, Y. Iijima, K. Kakimoto, T. Saitoh, S. Awaji, K. Watanabe, and Y. Shiohara, "Critical current properties in HTS tapes," *Phys. C-Supercond. Appl.*, vol. 392–396, pp. 1053–1062, Oct. 2003.
[51] V. Lombardo, *An* $I_c(B,\theta)$ *Parameterization for* $YBa_2Cu_3O_{7-\delta}$ *CC Tapes*. Batavia, IL: Fermilab Tech. Publ., May 2010, pp. 1–14.
[52] H. H. Song, F. L. Hunte, and J. Schwartz, "On the role of pre-existing defects and magnetic flux avalanches in the degradation of YBa2Cu3O7-x coated conductors by quenching," *Acta Materialia*, to be published.
[53] A. Ishiyama, Y. Nishio, H. Ueda, N. Kashima, M. Mori, T. Watanabe, S. Nagaya, M. Yagi, S. Mukoyama, T. Machi, and Y. Shiohara, "Degradation characteristics of YBCO-coated conductors subjected to overcurrent pulse," *IEEE Trans. Appl. Supercond.*, vol. 19, no. 3, pp. 3483–3486, Jun. 2009.

Wan Kan Chan (M'11) received the Ph.D. degree in applied and computational mathematics from Florida State University, Tallahassee, in 2007.

He then joined the National High Magnetic Field Laboratory and the Department of Mechanical Engineering, Florida State University, as a Postdoctoral Research Associate. He is currently a Research Scholar with the Department of Materials Science and Engineering, North Carolina State University, Raleigh, working on modeling of quench in high-temperature-superconducting-coated conductors and coils. His research interests include computational modeling of physical phenomena, particularly in the area of applied superconductivity, and numerical methods used in modeling.

Justin Schwartz (M'91–SM'01–F'04) received the B.S. degree from the University of Illinois at Urbana-Champaign, Urbana, in 1985 and the Ph.D. degree from Massachusetts Institute of Technology, Cambridge, in 1990.

After serving as one of the first Science and Technology Agency of Japan Fellows at the National Research Institute for Metals, Japan, he joined the University of Illinois at Urbana-Champaign, as an Assistant Professor. In 1993, he joined the newly formed National High Magnetic Field Laboratory and the Department of Mechanical Engineering, Florida State University, where he served as the Leader of the High-Temperature Superconductivity Magnets and Materials Group and the Coleader of the cluster hiring initiative in materials. In 2003, his research group established the world record for magnetic-field generation by a superconducting material. Since 2009, he has been the Head of the Department of Materials Science and Engineering and a Kobe Steel Distinguished Professor with North Carolina State University, Raleigh. His research interests include superconducting materials, multiferroic materials, and other functional oxides, with emphases on performance-limiting mechanisms, manufacturing-relevant processing techniques, and failure mechanisms, which he studies through experimental and microstructurally driven computational research.

Dr. Schwartz is the Editor-in-Chief of the IEEE TRANSACTIONS ON APPLIED SUPERCONDUCTIVITY.